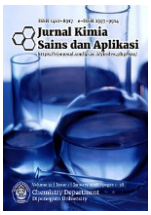
ISSN: 1410-8917
Jurnal Kimia Sains & Aplikasi
e-ISSN: 2597-9914

Jurnal Kimia Sains dan Aplikasi 29 (9) (2026): 590-607

Jurnal Kimia Sains dan Aplikasi
Journal of Scientific and Applied Chemistry

Journal homepage: http://ejournal.undip.ac.id/index.php/ksa



Synthesis, Structure, Hirshfeld Surface Analysis, and Antibacterial Activity of Monomeric Co(II) and Polymeric Ni(II) Complexes with 3-aminopyridine (3-ampy) and Benzoate Ion (Bz) Ligands as Antibacterial Agents

Siti Nur Lailatul Fitriyah [1], Nobitza Shafa Zafira [1], Meyga Evi Ferama Sari [1,*], I Wayan Dasna [1], Husni Wahyu Wijaya [1], Danar [1]

[1] Department of Chemistry, Faculty of Mathematics and Natural Sciences, Universitas Negeri Malang, Malang, Indonesia

* Corresponding author: meyga.evi.fmipa@um.ac.id

https://doi.org/10.14710/jksa.29.9.590-607

Article Info

Article history:

Received: 08th November 2025
Revised: 30th September 2026
Accepted: 05th October 2026
Online: 30th October 2026

Keywords:
Co(II) complex; Ni(II) complex; 3-aminopyridine; benzoate; antibacterial activity

Abstract

This study aimed to synthesize two new complexes, $[Co(3\text{-ampy})_2(Bz)_2(H_2O)]$ (**1**) and $[Ni(\mu\text{-}3\text{-ampy})_2(Bz)_2(H_2O)]_n$ (**2**), as antibacterial agents (3-ampy = 3-aminopyridine; Bz = benzoate). The complexes were synthesized by reacting cobalt(II) chloride or nickel(II) chloride with 3-ampy and sodium benzoate at a molar ratio of 1:2:2. The reactions were stirred at 40°C for 4 h and 3.5 h, respectively. The products were characterized using melting point analysis, electrical conductivity measurements, ATR-FTIR, SEM-EDX, SC-XRD, and UV–Vis spectroscopy. Hirshfeld surface analysis and antibacterial assays were also performed against *Escherichia coli* (ATCC 25922) and *Staphylococcus aureus* (ATCC 23235) using the disc diffusion method. Complexes **1** and **2** formed elongated prismatic red crystals and plate-shaped dark green crystals, respectively. Their melting points were 127–129°C and 224–226°C, respectively, and both were non-electrolytes in methanol. Complex **1** exhibited distorted octahedral geometry and crystallized in the monoclinic system, with benzoate ions coordinating in monodentate and bidentate modes. Its coordination environment was associated with *d–d* and ligand-to-metal charge-transfer (LMCT) bands in the UV–Vis spectrum. At equal mass concentrations, the complexes exhibited antibacterial activity with inhibition zones of 4.90–13.67 mm, whereas the free ligands showed no activity. Complex **1** inhibited *E. coli* and *S. aureus*, with inhibition zones of 12.20 and 13.67 mm, respectively. In contrast, complex **2** showed limited activity against *E. coli* (4.90 mm) and no activity against *S. aureus* (0.00 mm). The cobalt(II) complex exhibited broader antibacterial activity than the nickel(II) complex against the tested bacterial strains.

1. Introduction

Antimicrobial resistance (AMR) is a major global health concern that threatens the effective treatment of bacterial infections [1]. In Indonesia, antibiotic resistance in hospital populations was estimated to cause 34,530–133,753 deaths in 2019 [2], while bacterial AMR was associated with approximately 1.27 million deaths worldwide in the same year [3]. The emergence and spread of resistance are associated with inappropriate antibiotic use, inadequate infection prevention, and unequal access to quality and affordable medicines [4]. Among the major bacterial pathogens contributing to AMR-related deaths are *Escherichia coli* (*E. coli*) and *Staphylococcus aureus* (*S. aureus*), as well as *Klebsiella pneumoniae*, *Streptococcus pneumoniae*, *Acinetobacter baumannii*, and *Pseudomonas aeruginosa*. Methicillin-resistant *S. aureus* and several Gram-negative bacteria resistant to commonly used antibiotics contribute substantially to mortality worldwide [3]. These challenges highlight the need to investigate alternative

antibacterial agents with potential activity against resistant bacteria.

Conventional antibiotics, including ampicillin, amoxicillin, cefuroxime, and tetracycline, are commonly used to treat bacterial infections [5]. However, the development of bacterial resistance can reduce their effectiveness through various resistance mechanisms [6, 7]. Consequently, exploring compounds with different chemical properties and potential modes of antibacterial action is important. Metal complexes have attracted interest as potential antibacterial agents because their biological activity can be influenced by the metal center, ligand characteristics, coordination geometry, and physicochemical properties [1, 8]. Proposed mechanisms of metal-complex activity include interactions with cellular components, disruption of membrane function, interference with enzyme activity, and damage to DNA [9]. According to Tweedy's chelation theory, coordination can reduce the effective polarity of a metal ion through charge distribution and electron delocalization within the chelate ring. This may increase the lipophilic character of a complex and facilitate its interaction with lipid membranes [10]. Nevertheless, increased lipophilicity does not necessarily produce greater antibacterial activity, because molecular size, structural features, diffusion, and cellular interactions may also influence the observed effects.

Cobalt(II) and nickel(II) are suitable metal centers for investigating the relationship between coordination structure and antibacterial activity. Cobalt is biologically relevant as a component of vitamin B12, which functions as a cofactor in processes including fatty acid metabolism, DNA synthesis, and energy production [11]. Nickel(II), meanwhile, can coordinate with nitrogen and oxygen donor atoms, producing diverse coordination geometries and structural arrangements, including polymeric architectures. Previous studies have reported antibacterial activity in complexes containing these metals, although the activity depends on the ligands and coordination environments. A nickel(II) complex containing 1,3-bis(diphenylphosphino)propane and 2-aminopyridine (2-ampy) exhibited notable antibacterial properties compared with related Cu(II), Mn(II), and Fe(II) complexes [12].

Munadhiroh *et al.* [13] reported that $[Co(2\text{-ampy})_2(NCS)_2]$ exhibited greater antibacterial activity than KSCN against *S. aureus* and *Salmonella typhi*, although its activity relative to 2-ampy varied between bacterial species. Similarly, Savitri *et al.* [14] found that $[Co(4\text{-ampy})_4(NCS)_2]\cdot CO_2$ showed greater activity than KSCN but lower activity than 4-ampy. These findings demonstrate that complex formation does not invariably enhance antibacterial activity. Although Cu(II) and Zn(II) are also relevant in bioactive coordination compounds, differences in electronic configurations and coordination preferences can lead to distinct structures and biological responses [15]. Accordingly, Co(II) and Ni(II) were selected to investigate how different metal centers and coordination environments influence complex structure and antibacterial activity, rather than to assume their superiority over other metals [16].

Aminopyridine (ampy) isomers, including 2-ampy, 3-aminopyridine (3-ampy), and 4-ampy, are useful ligands in coordination chemistry because the pyridine nitrogen atom can donate a lone pair of electrons to a metal center [17]. Their aromatic ring systems can also participate in electronic interactions with coordinated metals [18]. The position of the amino group distinguishes these isomers and may influence ligand orientation, steric effects, and intermolecular interactions. In 2-ampy, the amino group is adjacent to the pyridine nitrogen, whereas in 4-ampy it occupies the para position. In 3-ampy, the amino group is located at the meta position, spatially separating it from the pyridine nitrogen. This arrangement may allow the pyridine nitrogen to act as the principal coordination site while the amino group contributes to secondary interactions, including hydrogen bonding. Previous studies have associated differences in amino-group position with variations in the crystal structures of metal–ampy complexes [19]. Furthermore, hydrogen bonding involving 3-ampy may influence crystal packing and the resulting structural arrangement [20]. These characteristics make 3-ampy a useful ligand for examining the relationship between coordination behavior, secondary interactions, and crystal architecture.

In the present study, the cobalt(II) and nickel(II) complexes exhibit different coordination architectures despite containing the same principal organic ligand. The complex $[Co(3\text{-ampy})_2(Bz)_2(H_2O)]$ (**1**) forms a monomeric structure, whereas $[Ni(\mu\text{-}3\text{-ampy})_2(Bz)_2(H_2O)]_n$ (**2**) forms a polymeric structure in which 3-ampy bridges nickel(II) centers. This structural difference provides an opportunity to investigate how metal identity and coordination connectivity influence the resulting crystal architecture and physicochemical properties. Benzoate (Bz) was selected as a co-ligand because benzoate-containing compounds have been investigated for their biological properties, while sodium benzoate is also used as a preservative in food and pharmaceutical applications [21]. However, the antibacterial effects of sodium benzoate itself do not establish the activity of its metal complexes, which must be evaluated experimentally.

Therefore, this study aimed to synthesize and characterize $[Co(3\text{-ampy})_2(Bz)_2(H_2O)]$ (**1**) and $[Ni(\mu\text{-}3\text{-ampy})_2(Bz)_2(H_2O)]_n$ (**2**), investigate their structural features using crystallographic and spectroscopic techniques, analyze their intermolecular interactions through Hirshfeld surface analysis, and evaluate their antibacterial activity against *E. coli* and *S. aureus*. Comparing the monomeric cobalt(II) complex with the polymeric nickel(II) complex provides insight into the relationship between metal identity, coordination architecture, and antibacterial activity.

2. Experimental

This experimental study consisted of four stages: (1) synthesis of the metal complexes, (2) characterization using melting point analysis, electrical conductivity measurements, ATR-FTIR, SEM-EDX, SC-XRD, and UV–

Vis spectroscopy, (3) antibacterial activity testing, and (4) Hirshfeld surface analysis.

2.1. Equipment and Materials

The equipment used in this study included an analytical balance (Ohaus, PA214, 0.0001 g readability, 210 g capacity), standard laboratory glassware, a hot plate magnetic stirrer (Thermo Scientific Cimarec, SP131320-33Q), a melting point apparatus (Fisher-Johns Melting Point Apparatus), a conductivity meter (Cyberscan CON 11/110), an FTIR-ATR spectrometer (Shimadzu, IRSpirit-X), an SEM-EDX instrument (FEI, Inspect-S50), an SC-XRD diffractometer (Bruker, D8 Quest Eco), and a UV-Vis spectrophotometer (Analytik Jena, Specord 200 Plus).

The materials used in this study included $CoCl_2{\cdot}6H_2O$ (Sigma-Aldrich, 31277, analytical grade, 98%), $NiCl_2{\cdot}6H_2O$ (Merck, analytical grade, 98%), 3-$NH_2C_5H_4N$ (Sigma-Aldrich, A78209, analytical grade, 99%), C_6H_5COONa (Sigma-Aldrich, 109169, 99%), nutrient broth (Himedia, M002), nutrient agar (Himedia, M001), methanol (Supelco, 106009, for analysis, ≥99.9%), ethanol (Merck, 1.00983.2500, absolute for analysis, ≥99.9%), dimethyl sulfoxide (DMSO; Merck, 1.02952.2500, ≥99.9%), demineralized water (Hydrobatt), and distilled water. The bacterial strains used were *Escherichia coli* (ATCC 25922) and *Staphylococcus aureus* (ATCC 23235). All chemicals were used as received without further purification.

2.2. Synthesis of Complex Compounds

2.2.1. Synthesis of Complex 1

$CoCl_2{\cdot}6H_2O$ (0.2428 g, 1 mmol) was dissolved in 5 mL of a methanol–water mixture (1:1, v/v) and stirred at 40°C. A solution of sodium benzoate (C_6H_5COONa; 0.2911 g, 2 mmol) in 5 mL of the same solvent mixture was added dropwise to the cobalt(II) solution. The mixture was stirred and heated at 40°C for 2 h [22]. Subsequently, a solution of 3-aminopyridine (3-ampy; 0.1901 g, 2 mmol) in 5 mL of methanol–water (1:1, v/v) was added dropwise. The mixture was then stirred and heated at 40°C for another 2 h. After cooling to room temperature, the mixture was filtered, and the filtrate was transferred to a 50 mL beaker. The beaker was covered with aluminum foil secured with rubber bands, with a small hole in the cover to allow slow solvent evaporation.

2.2.2. Synthesis of Complex 2

$NiCl_2{\cdot}6H_2O$ (0.2425 g, 1 mmol) was dissolved in 5 mL of an ethanol–water mixture (1:1, v/v). A solution of sodium benzoate (C_6H_5COONa; 0.2911 g, 2 mmol) in 5 mL of the same solvent mixture was added to the nickel(II) solution in a three-necked round-bottom flask. The mixture was stirred using a magnetic stirrer and heated at 40°C for 30 min until the solids had dissolved. Subsequently, a solution of 3-aminopyridine (3-ampy; 0.1901 g, 2 mmol) in 5 mL of ethanol–water (1:1, v/v) was added dropwise. The mixture was stirred and heated at 40°C for 3 h. After cooling to room temperature, the mixture was filtered, and the filtrate was transferred to a 50 mL beaker. The beaker was covered with aluminum foil secured with rubber bands, with a small hole in the cover to allow slow solvent evaporation.

The synthesis conditions were optimized by varying the solvent system, temperature, stirring duration, and evaporation conditions to obtain single crystals suitable for SC-XRD analysis. The optimization procedure was based on a previously reported method for synthesizing metal complexes [23].

2.3. Characterization

2.3.1. Melting Point Determination

Melting points were determined for the synthesized complex and its corresponding reactants using dry crystals of the samples. A small quantity of the sample was placed on a glass slide, covered with a cover slip, and heated across a temperature range of 30–300°C (heating power setting: 50) [14]. The melting process was visually monitored through a magnifying lens, and the melting range was recorded from the initial onset of melting to complete liquefaction. A sharp melting range ($\Delta T \leq 2°C$) indicated compound purity [24]. The melting point of the synthesized complex was compared with those of the starting materials to confirm successful complexation.

2.3.2. Electrical Conductivity Measurement

Electrical conductivity measurements were performed on 10 mL methanol solutions (1.0 mg/mL) of the synthesized complex and its reactants [25]. Complete dissolution was verified to ensure the conductivity probe was fully immersed. The instrument was calibrated prior to measurement using a standard KCl solution at 1413 µS/cm. Measurements were conducted at room temperature until stable readings were obtained. The cell was thoroughly rinsed with distilled water before and after each run. Electrical conductivity data were evaluated qualitatively to assess the electrolytic or non-electrolytic nature of the complex in methanol [25].

2.3.3. ATR-FTIR Spectroscopy

The samples analyzed using the ATR-FTIR instrument were the synthesized complex crystals and their ligands. The solid samples were ensured to be dry before measurement. A small amount of each sample was then placed directly on the ATR crystal. The solid samples were pressed against the ATR crystal to ensure uniform contact, whereas the liquid samples were dropped onto the crystal surface. Measurements were performed at room temperature over a wavenumber range of 4000–500 cm^{-1} [26]. The ATR crystal was cleaned with acetone and lint-free tissue between measurements. The coordination mode of the carboxylate groups ($-COO^-$) was assigned based on the magnitude of the asymmetric-symmetric stretching separation, $\Delta\nu = \nu_{as}(COO^-) - \nu_s(COO^-)$. By comparison with ionic sodium benzoate (Na-Bz), a smaller splitting indicates a bidentate mode, whereas a significantly larger splitting denotes a monodentate mode [27].

2.3.4. SEM-EDX Analysis

Surface morphology and elemental composition were analyzed using SEM-EDX. Solvent-free crystals

(~0.1 g) were mounted on an SEM stub and sputter-coated with an Au–Pd conductive layer. SEM micrographs were recorded in secondary electron (SE) mode at an accelerating voltage of 20 kV, a working distance of 10.0–10.1 mm, and magnifications ranging from 50× to 500×. EDX microanalysis was performed over an area of 100 µm. Microscale surface irregularities and surface tilt relative to the incident electron beam introduce composition measurement uncertainties of up to 34% and 85%, respectively [28].

2.3.5. SC-XRD

The sample characterized using SC-XRD was a single crystal of the synthesized complex compound. A high-quality crystal with a suitable size (0.1–0.5 mm) and well-defined morphology was selected. The crystal was mounted on a nylon loop using Paratone oil as a supporting medium and measured at room temperature. The nylon loop was then mounted on an X-ray diffractometer equipped with a Mo Kα X-ray source (λ = 0.71073 Å), a detector, and a goniometer. The crystal was oriented to allow rotation so that diffraction data could be collected from different crystallographic directions. X-rays were then directed at the crystal, and the diffracted beams at various angles were recorded by the detector.

2.3.6. UV-Vis Spectroscopy

The samples analyzed using the UV–Vis spectrophotometer were solutions of the synthesized complex compounds and their constituent metals. A 0.005 g sample was weighed and dissolved in 10 mL of methanol to obtain a concentration of 500 ppm. Subsequently, 1 mL of this solution was diluted to a final volume of 10 mL with methanol to obtain a concentration of 50 ppm. The samples were then measured at room temperature over a wavelength range of 190–1100 nm, with a scan speed of 50 nm/s, a data interval of 1 nm, and the absorbance mode selected.

2.4. Antibacterial Activity Test

Antibacterial activity was evaluated against Gram-negative *E. coli* (ATCC 25922) and Gram-positive *S. aureus* (ATCC 23235) using the disk diffusion method adapted from the Kirby–Bauer method, with reference to the *Performance Standards for Antimicrobial Disk Susceptibility Tests*, CLSI M02-Ed14 guidelines [29, 30]. The procedure encompassed bacterial suspension preparation, agar surface inoculation, application of compound-impregnated paper disks, incubation, and measurement of inhibition zone diameters. Standard CLSI conditions were modified to optimize media type and inoculum density. Consequently, inhibition zone diameters were used solely for relative activity comparisons among samples, rather than for clinical breakpoint or quality control (QC) range interpretations.

E. coli ATCC 25922 served as a standard reference strain for disk diffusion quality control. Although *S. aureus* ATCC 25923 is conventionally used for quality control testing, *S. aureus* ATCC 23235 (strain 494) was selected for this study. ATCC 23235 is an enterotoxin D-producing prototype strain originally isolated from a food poisoning outbreak, making it uniquely relevant for studying pathogenic *S. aureus* virulence [31]. The inclusion of ATCC 23235 was intended as a target test strain rather than a standard quality-control reference; thus, its inhibition zone diameters were evaluated strictly for comparative activity and were not benchmarked against the established quality-control parameters for ATCC 25923.

Bacterial strains were suspended in nutrient broth, stirred, and monitored spectrophotometrically at λ = 600 nm (OD600). Adjustments were made iteratively until an OD600 of 0.4–0.6 was achieved, confirming that cultures had reached the appropriate growth phase for testing [32]. The standardized bacterial suspension was inoculated into molten nutrient agar, then poured into Petri dishes and allowed to solidify. Test solutions comprised synthesized complexes **1** and **2**, precursor salts ($CoCl_2$, $NiCl_2$), ligands (3-ampy, Na-Bz), a positive control (chloramphenicol), and a negative control (10% v/v aqueous DMSO).

Samples (0.025 g) were dissolved in 5 mL of 10% DMSO to yield a mass concentration of 5.0 mg/mL. Because molar masses varied across test species, equivalent mass concentrations yielded differing molar concentrations (detailed in Table 9 to support comparative interpretation). Sterile paper disks were saturated with the respective test solutions for 20 min, placed onto the inoculated agar surface, and incubated at 37°C for 24 h. Because the mass of solution absorbed per disk was not measured gravimetrically or volumetrically, absolute disk loading µg/disk was not calculated directly. Post-incubation, inhibition zone diameters were measured in millimeters using a vernier caliper [25].

2.5. Hirshfeld Surface Analysis

Hirshfeld surface calculations and 2D fingerprint plots were generated using CrystalExplorer 21.5 based on SC-XRD structural data imported from refined Crystallographic Information Files (CIF) [14, 23]. Molecular surfaces were mapped using the normalized contact distance (d_{norm}), shape index, and curvedness to visually quantify and assess noncovalent intermolecular interactions.

3. Results and Discussion

3.1. Synthesis of Complex Compounds

Slow evaporation of a methanol solution containing precursor salts and ligands yielded single crystals suitable for characterization. Red, elongated prismatic crystals of **1** with pointed terminations were obtained after 4 days of ambient evaporation (Figure 1a). In contrast, dark green plate-like crystals of **2** formed after a longer crystallization period of 7 days (Figure 1b).

3.2. Characterization

3.2.1. Melting Point Determination

Based on the data in Table 1, the synthesized complex crystals exhibited a melting point range of 2°C, distinct from that of the reactants. This finding suggests that the synthesized products are pure compounds that differ from their reactants [13]. The substantial difference in

melting points between complexes **1** and **2** (approximately 97°C) suggests that the interactions within the crystal structure of complex **2** are relatively stronger, resulting in greater thermal stability than that of complex **1**. Compounds with stronger interactions within their crystal lattices require more thermal energy to overcome these interactions, resulting in higher melting points and reflecting greater lattice energy [33].

3.2.2. Electrical Conductivity Analysis

Electrical conductivity testing was conducted to evaluate the electrolytic behavior and species dissociation of complexes **1** and **2** in methanol solutions (Table 2) [25]. The conductivity data show that the synthesized complex compounds exhibit conductivity values closer to those of methanol and 3-ampy than to those of their constituent salts ($CoCl_2$, $NiCl_2$, and Na-Bz). This suggests that the complex compounds do not dissociate extensively in methanol and therefore produce relatively few free ions. Accordingly, the conductivity measurements indicate that complexes **1** and **2** exhibit non-electrolytic behavior in methanol solution [34].

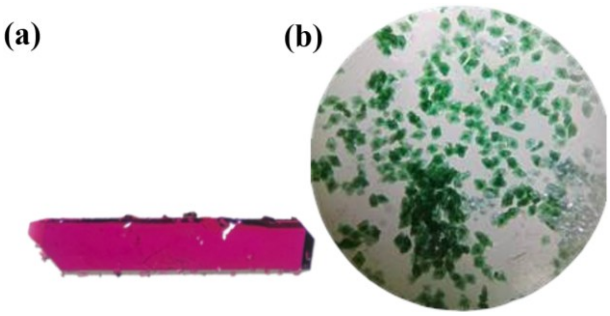


Figure 1. Crystals: (a) complex **1** displaying elongated prismatic morphology (5× magnification) and (b) complex **2** exhibiting plate-like morphology (1× magnification)

Table 1. Melting points of starting materials and synthesized complexes

Compound	Melting point (°C)
$CoCl_2{\cdot}6H_2O$	56
$NiCl_2{\cdot}6H_2O$	140
3-ampy	60–63
Na-Bz	>300
$[Co(3\text{-ampy})_2(Bz)_2(H_2O)]$ (**1**)	127–129
$[Ni(\mu\text{-}3\text{-ampy})_2(Bz)_2(H_2O)]_n$ (**2**)	224–226

Table 2. Electrical conductivity data for the solvent, reactants, and complex compounds

Solution	Value (µS)
Methanol (pure)	0.76
$CoCl_2(CH_3OH)$	484
$NiCl_2(CH_3OH)$	433
3-ampy(CH_3OH)	2.39
Na-Bz(CH_3OH)	379
$[Co(3\text{-ampy})_2(Bz)_2(H_2O)](CH_3OH)$ (**1**)	89.3
$[Ni(\mu\text{-}3\text{-ampy})_2(Bz)_2(H_2O)]_n(CH_3OH)$ (**2**)	82.0

3.2.3. ATR-FTIR Analysis

ATR-FTIR analysis was performed to identify the functional groups coordinating with the central metal atom in the complex compounds. The resulting FTIR spectra provide information on the characteristic absorption bands and their corresponding wavenumbers. The absorption bands of the synthesized complex compounds were compared with those of the corresponding free ligands, as shown in Figures 2–3 and Table 3.

The free 3-ampy ligand exhibits an asymmetric N–H stretching vibration (ν_{as}(N–H)) at 3373 cm^{-1}. In the spectra of complexes **1** and **2**, this band undergoes a red shift to 3345 cm^{-1} and 3331 cm^{-1}, respectively, signaling an overall weakening of the N–H bond due to coordination effects [25]. The larger red shift in **2** suggests the involvement of the amino nitrogen (N-amino) in coordination with the central Ni(II) ion. Concurrently, the C=N stretching vibration of the pyridine ring shifts from 1653 cm^{-1} in free 3-ampy to 1645 cm^{-1} in **1** and 1619 cm^{-1} in **2**. The larger shift observed in **2** ($\Delta\nu$ = 34 cm^{-1}) compared to 1 ($\Delta\nu$ = 8 cm^{-1}) indicates a significant alteration of the electronic structure within the pyridine ring, reflecting different coordination environments and ligand-metal binding modes between the two complexes. Additionally, the C–NH_2 stretching vibration of the pyridine moiety shifts from 1288 cm^{-1} in free 3-ampy to 1308 cm^{-1} (**1**) and 1307 cm^{-1} (**2**) [13, 17].

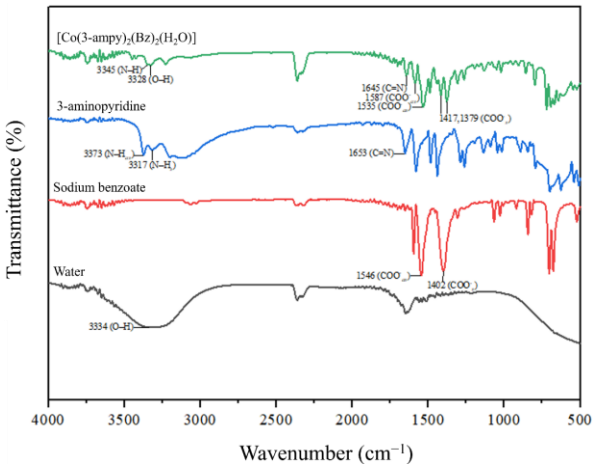


Figure 2. FTIR spectra of complex **1** and its ligands

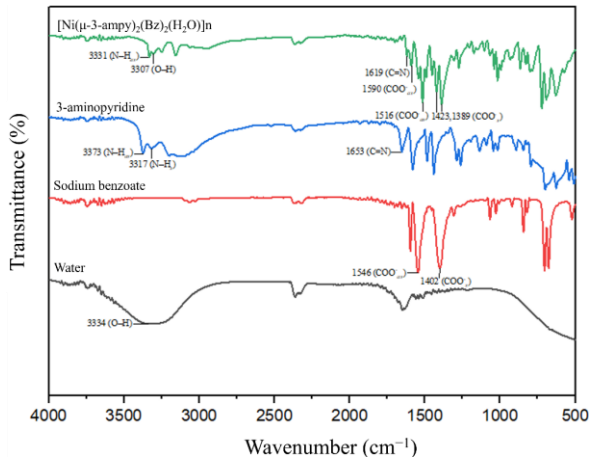


Figure 3. FTIR spectra of complex **2** and its ligands

Table 3. Infrared absorption band assignments for complexes 1 and 2 relative to their precursor ligands

Vibrational mode	Wavenumber (cm^{-1})				
	Ligand			Complex compounds	
	3-ampy	Na-Bz	H_2O	$[Co(3\text{-ampy})_2(Bz)_2(H_2O)]$ (**1**)	$[Ni(\mu\text{-}3\text{-ampy})_2(Bz)_2(H_2O)]_n$ (**2**)
$\nu_{as}(N-H)$	3373	-	-	3345	3331
$\nu(O-H)$	-	-	3334	3328	3307
$\nu_s(N-H)$	3317	-	-	-	-
$\nu(C-H)$	3070	-	-	3062	3061
$\delta(H-O-H)$	-	-	1653	1683	1653
$\nu(C=N)$	1653	-	-	1645	1619
$\nu_{as}(COO^-)$	-	1546	-	1587	1590
ν(ring)	1581	1596	-	-	1542
$\nu_{as}(COO^-)$	-	1546	-	1535	1516
ν(ring)	1485	-	-	1490	1491
ν(ring)	1440	-	-	1442	1451
$\nu_s(COO^-)$	-	1402	-	1417	1423
$\nu_s(COO^-)$	-	1402	-	1379	1389
$\nu(C-NH_2)$	1288	-	-	1308	1307
ν(ring)	1262	-	-	1265	1274
ν(ring breathing)	1045	1067	-	1052	1067

Coordination modes of the carboxylate group ($-COO^-$) were deduced from the separation ($\Delta\nu$) between the asymmetric ($\nu_{as}(COO^-)$) and symmetric ($\nu_s(COO^-)$) stretching frequencies. Free sodium benzoate (Na-Bz) displays $\nu_{as}(COO^-)$ and $\nu_s(COO^-)$ bands at 1546 cm^{-1} and 1402 cm^{-1}, respectively ($\Delta\nu$ = 144 cm^{-1}). For complex **1**, two distinct coordination modes are observed: a monodentate benzoate ligand characterized by stretching bands at 1587 cm^{-1} and 1379 cm^{-1} ($\Delta\nu$ = 208 cm^{-1}), and a bidentate mode at 1535 cm^{-1} and 1417 cm^{-1} ($\Delta\nu$ = 118 cm^{-1}). Similarly, complex **2** exhibits monodentate (1590 and 1389 cm^{-1}; $\Delta\nu$ = 201 cm^{-1}) and bidentate (1516 and 1423 cm^{-1}; $\Delta\nu$ = 93 cm^{-1}) coordination modes [26].

Water ligand coordination was confirmed by characteristic O–H stretching and bending vibrations. Free water exhibits an O–H stretching band at 3334 cm^{-1}, which shifts to lower wavenumbers (3328 cm^{-1} in **1** and 3307 cm^{-1} in **2**) upon coordination to the metal center [26]. Furthermore, the H–O–H bending vibration (δ(H–O–H)), observed at 1653 cm^{-1} in water, shifts to 1683 cm^{-1} in **1** while remaining at 1653 cm^{-1} in **2** [35].

3.2.4. SEM-EDX Analysis

SEM micrographs reveal distinct crystal morphologies for the synthesized complexes, as depicted in Figures 4a and 4b. Complex **1** exhibits pointed, rod-like elongated crystals, whereas complex **2** displays plate-like structures. These observed physical shapes align closely with the single-crystal habits identified during SC-XRD analysis.

The surface elemental compositions of both complexes were quantitatively assessed via EDX (Table 4). For complex **1**, the surface atomic ratio of Co:O:N was measured at 1:5.4:9.7 [36]. The relative Co:O atomic ratio closely corresponds to the presence of two benzoate anions ($C_6H_5COO^-$) and one water ligand (H_2O) per cobalt center, consistent with the structural formula derived from single-crystal XRD data. However, the detected nitrogen proportion deviates slightly from the theoretical stoichiometry. For complex **2**, the Ni:O:N atomic ratio on the crystal surface was found to be 1:7:7.6 [36], which also shows minor discrepancies compared to the SC-XRD crystallographic chemical formula.

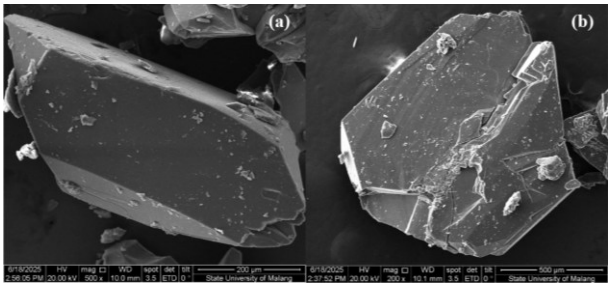


Figure 4. SEM micrographs of (a) complex **1** (500× magnification; scale bar = 200 µm; WD = 10.0 mm) and (b) complex **2** (200× magnification; scale bar = 500 µm; WD = 10.1 mm), acquired at an accelerating voltage of 20 kV in SE mode

Table 4. EDX surface elemental composition of synthesized complexes **1** and **2**

Compound	Element	%wt	%At
$[Co(3\text{-ampy})_2(Bz)_2(H_2O)]$ (**1**)	N	48.16	60.07
	O	30.87	33.71
	Co	20.97	6.22
$[Ni(\mu\text{-}3\text{-ampy})_2(Bz)_2(H_2O)]_n$ (**2**)	N	38.41	48.74
	O	40.34	44.82
	Ni	21.25	6.44

Table 5. Crystallographic data of complex compounds

Crystallographic parameter	[Co(3-ampy)$_2$(Bz)$_2$(H$_2$O)] (**1**)	[Ni(μ-3-ampy)$_2$(Bz)$_2$(H$_2$O)]$_n$ (**2**)
CCDC number	2455783	2442354
Empirical formula	$C_{24}H_{24}CoN_4O_5$	$C_{19}H_{18}N_2NiO_5$
Formula weight (g/mol)	507.40	413.04
Crystal system	Monoclinic	Monoclinic
Space group	$P2_1/n$ (14)	$P2_1/c$
a (Å)	9.7144(3)	13.4464(6)
b (Å)	20.8634(7)	9.4334(4)
c (Å)	12.0949(4)	14.4275(6)
$\alpha = \gamma$ (°)	90	90
β (°)	106.6960(10)	92.099(2)
Volume (Å^3)	2348.00(13)	1828.83(14)
Z	4	4
Total reflections collected	9896	6437
θ_{min}(°)	2.3968	2.5803
θ_{max}(°)	28.2346	23.3630
Temperature (K)	296(2)	296(2)
Crystal dimensions (mm)	0.35/0.30/0.28	0.25/0.20/0.18
Calculated density (g/cm^3)	1.435	1.500
$F_{(000)}$	1052	856
Absorption coefficient (mm^{-1})	0.774	1.094
Absorption correction type	Multi-Scan	Multi-Scan
T_{min}; T_{max}	0.5947; 0.7457	0.611082; 0.745332
Radiation type	Mo Kα	Mo Kα
Radiation wavelength (Å)	0.71073	0.71073
Index ranges (h, k, l_{max})	12, 27, 16	16, 11, 17
$R1$ (I > 2σ(I))	0.0330	0.0340
$wR2$	0.0804	0.0641
Goodness-of-fit on F2	1.051	1.034
Data/parameters/restrains	5794/307/0	3650/251/25

These stoichiometric deviations can be attributed primarily to surface impurities and morphology-induced measurement artifacts. During slow evaporation of the solvent during the synthesis of complex **2**, trace amounts of a light green byproduct, identified as Ni(C$_6$H$_5$COO)$_2$, co-precipitated alongside the target compound. Furthermore, surface topographies such as microscale indentations, cracks, and protrusions heavily influence X-ray emission and absorption. Microscale surface irregularities scatter characteristic X-rays unevenly, introducing elemental composition uncertainties of up to 34% from theoretical values [28].

3.2.5. SC-XRD Analysis

Crystallographic data and structural refinement parameters for complexes **1** and **2** are summarized in Table 5. Both compounds crystallize in the monoclinic crystal system, with complex **1** belonging to the space group P2$_1$/n and complex **2** to P2$_1$/c. Structural refinement was performed using the APEX4 software suite, and molecular graphic representations were generated using Mercury 4.2.0.

The structure of complex **1** in Figure 5 shows that the central Co(II) ion is coordinated to four O atoms from the benzoate and water ligands and two N atoms from the 3-ampy ligands, forming a distorted octahedral geometry. The IR spectrum of the complex exhibits characteristic bands associated with the O–H groups of the coordinated water molecule, the C=N and C–NH$_2$ groups of 3-ampy, and the COO$^-$ groups of the benzoate ligands. These findings demonstrate good agreement between the FTIR and SC-XRD results. The water and 3-ampy ligands act as monodentate ligands, whereas benzoate can coordinate in either a monodentate or a bidentate mode. Furthermore, Figure 5 shows that complex **1** contains no counterions, consistent with its conductivity data.

The Co:O atomic ratio determined by SEM–EDX was 1:5.4, while the crystal structure indicates that each Co(II) ion is coordinated to two benzoate ligands and one water molecule. The crystal packing of complex **1** within the unit cell is shown in Figure 6, which contains four molecules of the complex. These molecules are generated by four symmetry operations: identity (x, y, z), 2$_1$ screw axis $\left(\frac{1}{2}-x, \frac{1}{2}+y, \frac{1}{2}-z\right)$, inversion center $(-x, -y, -z)$, and n-

glide plane $\left(\frac{1}{2}+x,\frac{1}{2}-y,\frac{1}{2}+z\right)$ (Figure 7). The inversion operation is generated by the combination of the 2_1 screw-axis and *n*-glide-plane operations.

The crystal structure of complex **1** is stabilized by an intricate network of intramolecular and intermolecular hydrogen bonds (Figure 8). The primary hydrogen-bonding interactions include C=O···H–O, O–H···O, O···H–O, and O···H–N contacts. An intramolecular C=O···H–O bond occurs between the uncoordinated carboxylate oxygen of the monodentate benzoate ligand and a coordinated water hydrogen (O···H = 1.915 Å). Intermolecular O–H···O interactions (H···O = 2.030 Å) connect adjacent complexes through coordinated water and carboxylate oxygen atoms of the bidentate benzoate ligand. Additional O···H–N interactions (O···H = 2.082 Å) occur between the bidentate benzoate oxygen and amino hydrogens of the 3-ampy ligand. These N–H···O interactions may contribute to the red shift of the asymmetric N–H stretching band observed in the FTIR spectrum. The corresponding O···H/H···O contacts also appear as prominent spikes in the Hirshfeld surface analysis, highlighting their contribution to crystal packing.

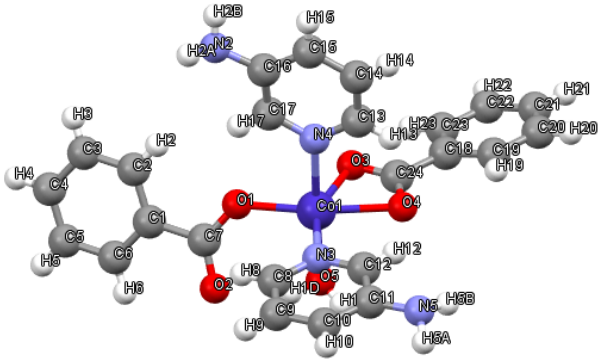


Figure 5. Structure of complex **1**

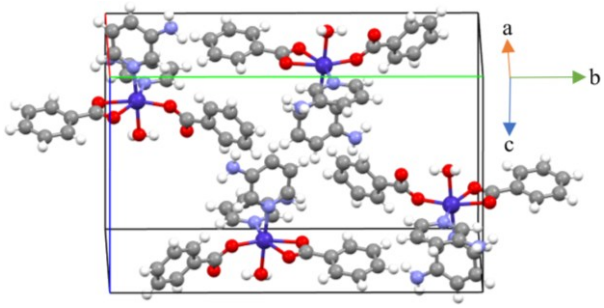


Figure 6. Crystal packing of complex 1 along the *a*-axis

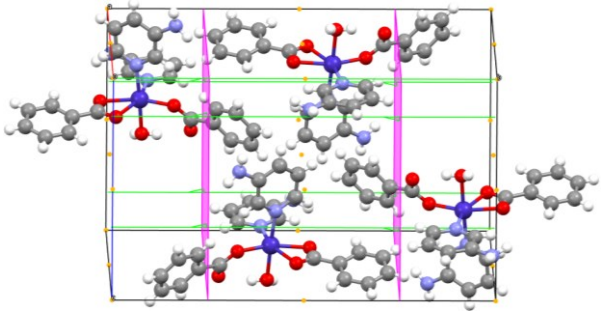


Figure 7. Visualization of the 2_1 screw-axis (green) and *n*-glide-plane (pink) symmetry operations in complex **1** along the *a*-axis

Table 6. Bond lengths and bond angles in complex **1**

Bond	Bond length (Å)	Bond angle	Angle (°)
Co1-O1	2.047(1)	O1-Co1-O3	101.76(5)
Co1-O3	2.188(1)	O1-Co1-O4	161.30(5)
Co1-O4	2.180(1)	O1-Co1-O5	89.54(5)
Co1-O5	2.150(1)	O3-Co1-O4	60.07(5)
Co1-N3	2.114(2)	O3-Co1-O5	88.74(5)
Co1-N4	2.149(1)	O4-Co1-O5	85.89(5)
		O1-Co1-N3	102.99(5)
		O1-Co1-N4	91.85(5)
		O3-Co1-N3	155.19(5)
		O3-Co1-N4	89.40(5)
		O4-Co1-N3	95.13(5)
		O4-Co1-N4	92.29(5)
		O5-Co1-N3	89.86(5)
		O5-Co1-N4	177.88(5)
		N3-Co1-N4	91.38(6)

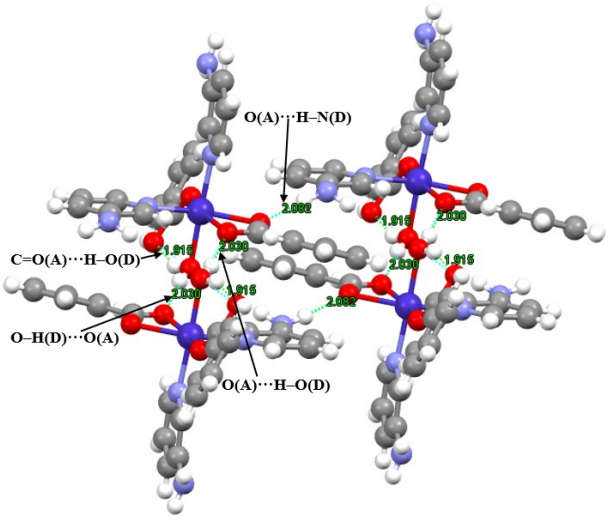


Figure 8. Intramolecular and intermolecular hydrogen-bonding interactions in complex **1**

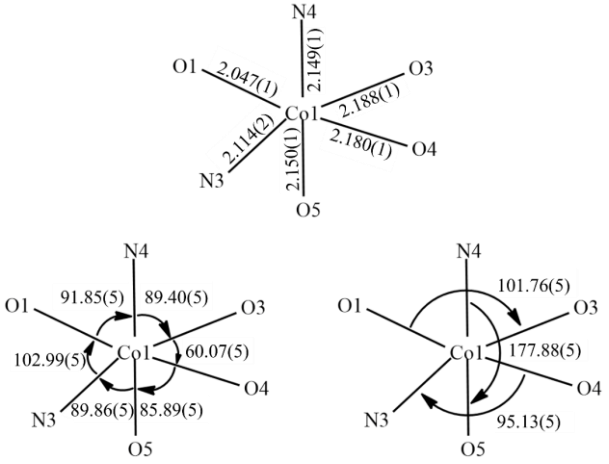


Figure 9. Illustration of the bond lengths and bond angles in the geometry of complex **1**

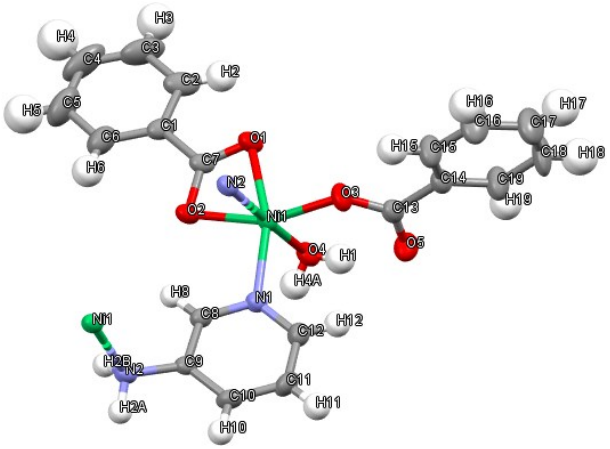


Figure 10. Asymmetric structure of complex **2**

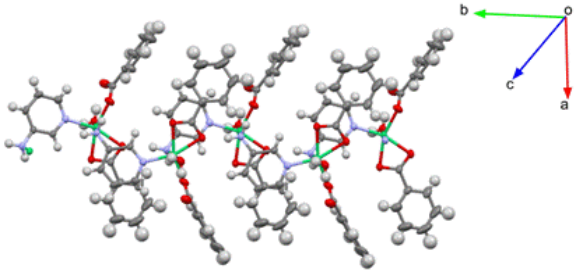


Figure 11. Polymer structure of complex **2**

Within the equatorial plane of complex 1, the Co–O and Co–N bond lengths show notable variations. The Co1–O3 and Co1–O4 bond lengths are similar at 2.188(1) and 2.180(1) Å, respectively, indicating symmetric chelation by the bidentate benzoate ligand. These bond distances are distinctly longer than the Co1–O1 (monodentate benzoate, 2.047(1) Å) and Co1–N3 (3-ampy, 2.114(2) Å) bonds, which is attributed to steric bite-angle constraints and electronic repulsion between the adjacent O3 and O4 donor atoms.

Furthermore, the Co1–N3 distance is longer than Co1–O1; this elongation stems from a smaller O4–Co1–N3 angle (95.13(5)°) compared to O1–Co1–O3 (101.76(5)°), bringing the pyridine ring into closer spatial proximity with the bidentate benzoate anion and increasing local steric repulsion [14]. In axial positions, the Co1–O5 (aqua) and Co1–N4 (3-ampy) bond lengths are almost identical at 2.150(1) Å and 2.149(1) Å, respectively. The axial O5–Co1–N4 angle of 177.88(5)° deviates slightly from linearity (180°), driven by structural distortions induced by intramolecular and intermolecular hydrogen bonding involving the water ligand. The complete set of bond lengths and angles listed in Table 6 and illustrated in Figure 9 confirms a distorted octahedral coordination geometry around Co(II).

The asymmetric unit of complex **2** consists of one nickel(II) ion, two bridging 3-ampy ligands, one monodentate benzoate anion, one bidentate benzoate anion, and one coordinated water ligand. As depicted in Figure 10, the monomeric unit of **2** features a distorted octahedral environment around the Ni(II) center surrounded by two 3-ampy ligands, one monodentate benzoate anion, one bidentate benzoate anion, and one water ligand. Similar to complex **1**, the coordination sphere is entirely neutral, lacking outer-sphere counterions, corroborating the experimentally determined non-electrolytic molar conductivity.

The polymeric framework of complex **2** is depicted in Figure 11. The Ni1–N1 and Ni1–N2 coordination bond lengths are 2.053 Å and 2.190 Å, respectively, with an N2–Ni1–N1 bond angle of 86.55°. The observed deviations in bond distances and angles from ideal octahedral parameters demonstrate substantial geometric distortion within the nickel(II) coordination sphere. This structural distortion arises from an interplay of factors, including heterogeneous ligand types, mixed coordination modes, interligand steric repulsion, and potentially weak Jahn–Teller effects associated with the high-spin d^8 electronic configuration [23].

The Ni^{2+} ion possesses an [Ar]3d^8 configuration, represented under octahedral crystal field theory as $t_{2g}^6 e_g^2$, containing two unpaired electrons in the doubly degenerate e_g orbitals. In such systems, geometric distortion lowers the overall energy by lifting orbital degeneracy, causing axial elongation or compression of metal–ligand bonds [37]. However, Jahn–Teller distortions in octahedral nickel(II) complexes are intrinsically weak and heavily modulated by the local ligand environment. Consequently, the coordination asymmetry in complex **2** should not be attributed solely to electronic Jahn–Teller effects, but rather understood as a consequence of ligand sterics and binding modes.

The coordination sphere of complex **2** comprises two bridging 3-ampy ligands, one monodentate benzoate anion, one bidentate benzoate anion, and one water ligand. The co-existence of these distinct ligand types induces structural asymmetry around the Ni(II) center. Furthermore, varying steric bulk and electron-donating properties among the ligands generate uneven interligand repulsions, directly causing variations in Ni–ligand bond lengths and angles. The 3-ampy moieties function as bis-monodentate bridging ligands, linking adjacent nickel(II) centers into an extended 1D coordination polymer chain (Figure 11). Thus, both the spatial arrangement of the diverse ligands and the connectivity of the polymeric backbone dictate the magnitude and direction of the geometric distortion surrounding the Ni(II) ions.

Within the polymeric network of complex **2**, aromatic rings are arranged in close spatial proximity, facilitating intermolecular π···π stacking interactions. These non-covalent interactions occur between electron-rich and electron-deficient aromatic π-systems. Nitrogen-containing heterocycles, such as 3-ampy, are electron-poor due to the strong electron-withdrawing nature of the pyridine nitrogen, rendering them susceptible to π-stacking with surrounding aromatic moieties [38]. Indeed, pronounced π···π stacking occurs between the π-systems of a 3-ampy ring and a bidentate benzoate ring on neighboring polymer chains. This interaction is characterized by a centroid-to-centroid distance of 3.770 Å (between the C1–C6 ring and the C8–C12/N1 ring) and an interplanar dihedral angle of 6.75° [26].

The short centroid separation confirms spatial proximity, while the small interplanar angle demonstrates near-parallel alignment of the aromatic rings. The lateral offset observed between the ring centers confirms a parallel-displaced (offset) stacking geometry. These intermolecular π···π stacking interactions play a pivotal role in stabilizing the supramolecular assembly, bridging individual 1D polymer chains into a cohesive, robust 3D crystal lattice alongside hydrogen-bonding networks [26].

Differences in bond lengths and angles around the nickel(II) center demonstrate asymmetric distortion from ideal octahedral geometry. Variations in bond lengths are observed along all three Cartesian axes. Along the z-axis, the Ni1–O4 bond undergoes compression, whereas the Ni1–N2 bond exhibits significant elongation [39]. Along the x-axis, the Ni1–N1 bond undergoes compression, while Ni1–O1 undergoes elongation. Concurrently, along the y-axis, the Ni1–O3 bond is compressed, whereas Ni1–O2 is elongated. The complete set of coordination bond distances and angles for complex **2** is summarized in Table 7.

Furthermore, individual C–O bond distances and O– C–O angles within the two benzoate ligands differ notably (Table 8). These differences are associated with the distinct coordination modes of the two benzoate ligands, which act as monodentate and bidentate ligands, respectively. The different coordination modes result in distinct geometries and coordination interactions around the nickel(II) center, leading to variations in the Ni–O bond lengths and O–Ni–O bond angles.

Table 7. Bond length and angle in complex **2**

Bond	Bond length (Å)	Bond angle	Angle (°)
Ni1–N1	2.053(2)	N1–Ni1–N2	86.55(8)
Ni1–N2	2.190(2)	N1–Ni1–O1	161.68(7)
Ni1–O1	2.148(2)	N1–Ni1–O4	93.35(8)
Ni1–O2	2.108(2)	N2–Ni1–O2	91.47(7)
Ni1–O3	2.002(2)	N2–Ni1–O3	83.21(7)
Ni1–O4	2.075(2)	N2–Ni1–O4	177.56(8)
		O1–Ni1–O2	61.88(6)
		O1–Ni1–O3	98.61(7)
		O1–Ni1–O4	88.39(7)
		O2–Ni1–O3	159.64(7)

Table 8. Bond length and angle of the benzoate ligand in complex **2**

Bond	Bond length (Å)	Bond	Angle (°)
C7–O1	1.262(3)	O1–C7–O2	119.5(2)
C7–O2	1.272(2)	O3–C13–O5	125.3(2)
C13–O3	1.260(3)		
C13–O5	1.246(3)		

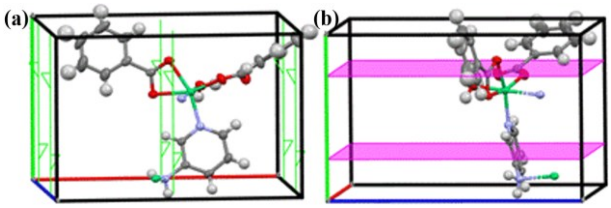


Figure 12. Visualization of symmetry operation (a) 2_1 screw axis and (b) *c*-glide plane

Complex **2** crystallizes in the monoclinic space group $P2_1/c$, describing the internal translational and rotational symmetry of its crystal lattice. The letter "P" denotes a primitive unit cell containing a single lattice point per cell. The "2_1" symbol indicates a two-fold screw axis (2_1 screw symmetry), comprising a 180° rotation followed by a fractional translation of $\frac{1}{2}$ along the *b*-axis. The "/c" symbol designates a *c*-glide plane perpendicular to the *b*- axis, involving a mirror reflection combined with a translation parallel to the c-axis by $\frac{1}{2}$ unit cell length (Figure 12).

Comparative evaluation of SC-XRD data confirms coordination of the pyridine nitrogen atom of 3-ampy to the metal centers in both compounds. The Co1–N3 bond length in complex **1** is 2.114 Å, whereas the corresponding Ni1–N1 bond length in complex **2** is shorter at 2.053 Å. This contraction reflects differences in ionic radii between Co(II) and Ni(II), as well as distinct ligand-field environments. The shorter Ni1–N1 bond in **2** indicates stronger metal–ligand orbital overlap and a shorter interatomic distance than the Co1–N3 bond in **1**. This altered coordination strength alters the electron density distribution within the 3-ampy heterocycle, directly correlating with the magnitude of the ν(C=N) stretching frequency shift observed in FTIR spectroscopy. Specifically, complex **2** exhibits a much larger ν(C=N) red shift ($\Delta\nu$ = 34 cm^{-1}) than complex **1** ($\Delta\nu$ = 34 cm^{-1}).

In addition to differences in the M–N bond lengths, SC-XRD analysis revealed structural differences between the two compounds. Complex 1 exhibits a monomeric structure, whereas complex **2** forms a coordination polymer. Consequently, the 3-ampy ligand in complex **2** experiences a different structural environment from that in complex **1**. The polymeric structure may contribute to changes in the electronic environment of the ligand, which may partly account for the greater shift of the ν(C=N) band toward lower wavenumbers in complex **2**. Therefore, the more pronounced redshift of the ν(C=N) band in complex **2** can be attributed to differences in coordination environment and crystal structure, with the shorter Ni1–N1 bond length and the formation of a coordination polymer potentially contributing to the altered electronic environment of the ligand.

3.2.6. UV-Vis Analysis

The electronic absorption spectra of the synthesized complexes in methanol solution were recorded and compared with those of the corresponding precursor metal salts (Figures 13–15). Optimization of sample concentrations at 50, 75, and 100 ppm demonstrated that 50 ppm yielded optimal spectral clarity, with well-

defined absorption bands and minimal signal noise. Concentrations of 75 and 100 ppm introduced significant baseline noise, degrading spectral resolution; thus, 50 ppm was selected for all spectroscopic measurements.

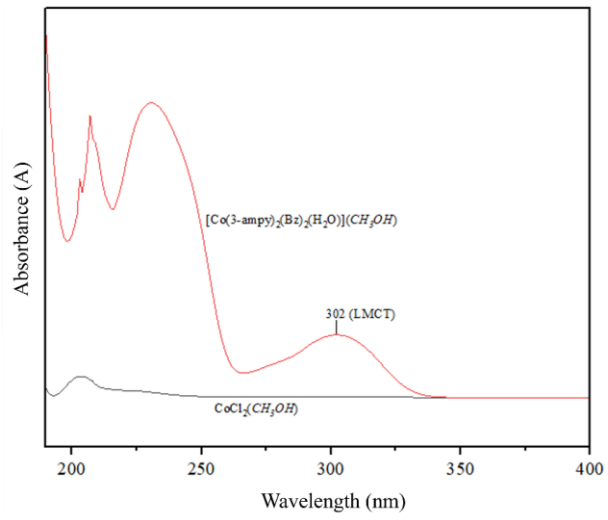


Figure 13. UV spectra of $CoCl_2$ solution and complex **1**

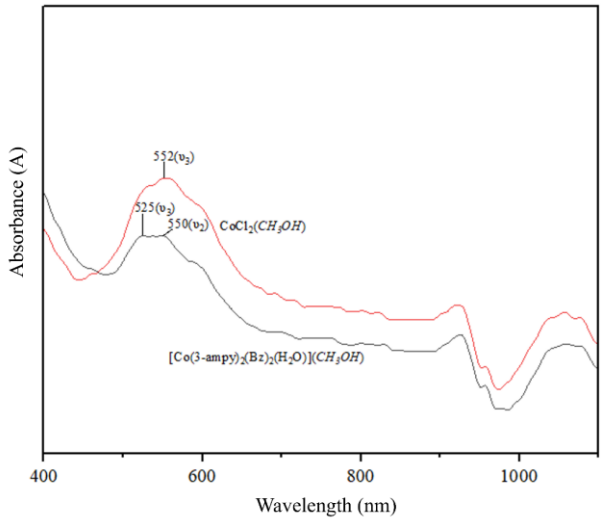


Figure 14. Vis spectra of $CoCl_2$ solution and complex **1**

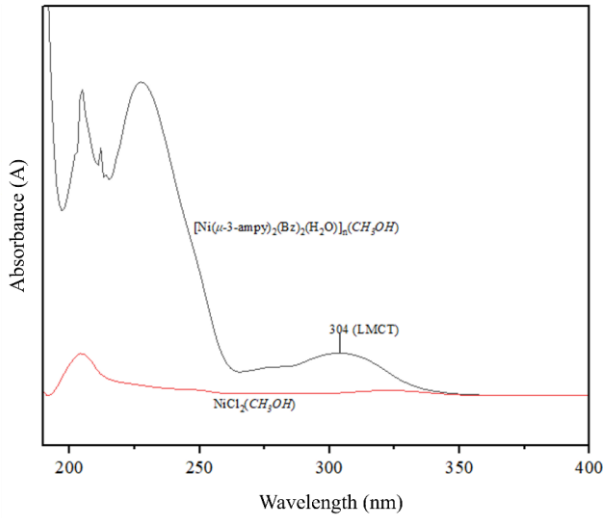


Figure 15. UV spectra of $NiCl_2$ solution and complex **2**

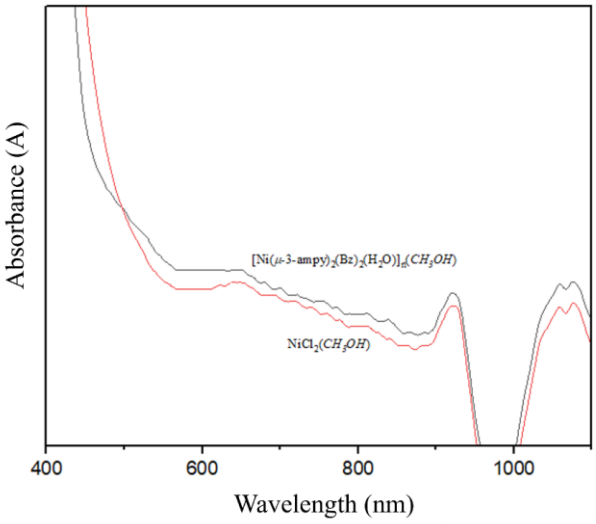


Figure 16. Vis spectra of $NiCl_2$ solution and complex **2**

As shown in Figure 14, the visible absorption bands recorded at ~525, ~550, and ~552 nm for $CoCl_2$ and complex **1** are attributed to spin-allowed *d*–*d* electronic transitions of the high-spin d^7 cobalt(II) ion [40]. In an octahedral crystal field, the *d*–*d* transitions of high-spin Co(II) are rationalized using the Tanabe-Sugano diagram, corresponding to transitions from the ground state $^4T_{1g}(F)$ to the excited states $^4T_{2g}(F)$ (ν_1), $^4A_{2g}(F)$ (ν_2), and $^4T_{1g}(P)$ (ν_3) [41]. In the visible region, the band at ~550 nm is assigned to the $^4T_{1g}(F) \rightarrow {}^4A_{2g}(F)$ (ν_2) transition, whereas the bands at ~525 and ~552 nm correspond to the $^4T_{1g}(F) \rightarrow {}^4T_{1g}(P)$ (ν_3) transition. The lowest-energy ν_1 transition ($^4T_{1g}(F) \rightarrow {}^4T_{2g}(F)$) occurs in the near-infrared region, exceeding the detection range of the spectrophotometer [41, 42].

In ideal centrosymmetric octahedral complexes, *d*–*d* transitions are Laporte-forbidden. However, distortion of the octahedral geometry reduces the local symmetry, relaxing the Laporte selection rule. Vibronic coupling can also partially relax this restriction, allowing formally forbidden *d*–*d* transitions to appear as weak absorption bands [43]. Thus, the weak bands observed at approximately 525, 550, and 552 nm are consistent with *d*–*d* transitions of high-spin d^7 Co(II) in a distorted octahedral coordination environment. Differences in band positions between $CoCl_2$ and complex **2** indicate changes in the coordination environment of Co(II) upon complex formation with 3-ampy and benzoate ligands. These changes affect the splitting of the Co(II) *d* orbitals and, consequently, the energies of the electronic transitions. The blue shift of the ν_3 band to a shorter wavelength indicates an increase in transition energy relative to the Co(II) precursor. This shift may be attributed to changes in the ligand-field strength and coordination environment upon complex formation.

In contrast, as illustrated in Figure 16, no well-defined *d*–*d* absorption bands were resolved in the visible region for $NiCl_2$ or complex **2**, instead displaying a featureless absorbance gradient. Meanwhile, the sharp absorbance variation in the 900–1000 nm region was not assigned to an electronic absorption band because it lacked a well-defined profile and may have been

attributable to limitations in the instrument response at these wavelengths. The absence of prominent *d*–*d* bands is typical for nickel(II) complexes, where weak *d*–*d* transitions often undergo significant band broadening or overlap with high-intensity charge-transfer tails [43]. Consequently, the coordination geometry of complex **2** was established primarily via SC-XRD analysis.

As shown in Figures 13 and 15, intense absorption bands at 302 and 304 nm are assigned to LMCT transitions, involving electron promotion from ligand-based orbitals to empty metal *d*-orbitals [26]. Unlike Laporte-forbidden *d*–*d* transitions, LMCT processes are fully spin- and parity-allowed, exhibiting significantly higher molar absorptivities and stronger absorption intensities in the UV region.

3.3. Antibacterial Activity Test

In vitro antibacterial activity of the synthesized complexes was evaluated against Gram-negative *E. coli* (ATCC 25922) and Gram-positive *S. aureus* (ATCC 23235) using a disk diffusion assay adapted from the Kirby-Bauer method, with testing performed in triplicate [14]. Aqueous 10% v/v DMSO served as the negative control, while chloramphenicol (30 µg/disk) was employed as the positive reference standard [14, 44]. All test samples were evaluated at a standardized mass concentration of 5.0 mg/mL in 10% DMSO. Antibacterial efficacy was determined by measuring the diameter of clear inhibition zones surrounding the disks. Representative clear zones and mean inhibition zone diameters (± standard deviation) are displayed in Figure 17 and Table 9.

Evaluating inhibition zone diameters at an equivalent mass concentration reflects relative antibacterial potency under identical mass loading, but does not directly correspond to equimolar comparisons due to variations in molecular weight. Molar concentration provides a more rigorous benchmark for comparing bioactivity among structurally distinct compounds. However, in disk diffusion assays, the magnitude of the inhibition zone is governed not only by molar concentration or dose per disk, but also by the intrinsic solubility and agar diffusion rate of each compound. Therefore, antibacterial activity in this study was evaluated by concurrently considering mass concentration, molar concentration, and molecular diffusion characteristics.

As indicated in Table 9, complexes **1** and **2** exhibited significantly smaller inhibition zone diameters than the positive control, chloramphenicol. Chloramphenicol is a broad-spectrum antibiotic featuring a *p*-nitrophenyl ring linked to a dichloroacetyl tail via a 2-amino-1,3-propanediol core. Its primary mode of action is to bind to the peptidyl transferase center of the 50S subunit of the bacterial ribosome, thereby inhibiting peptide bond formation by sterically impeding the entry of aminoacyl-tRNA into the A-site [45, 46].

Within the peptidyl transferase pocket, the nitrobenzene ring of chloramphenicol establishes π- stacking interactions with 23S rRNA nucleotide bases, inducing a conformational rotation (>120°) that facilitates hydrogen bonding with the drug's carbonyl group. Furthermore, the nascent peptide chain interacts directly via C–H···π contacts and hydrogen bonds with chloramphenicol's chlorine atom, while its methylene C4-hydroxyl group coordinates with active-site potassium ions. The concerted presence of these functional moieties (carbonyl, hydroxyl, chlorine, and nitrobenzene) enables tight ribosomal binding, culminating in robust inhibition of bacterial growth [45, 46].

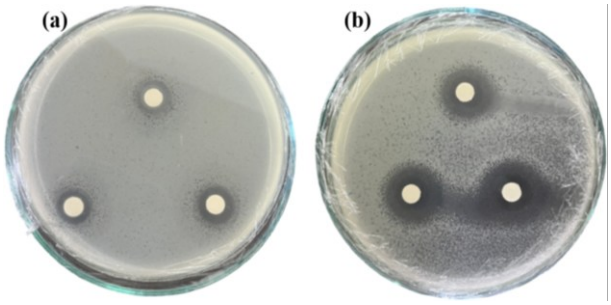


Figure 17. Inhibition zone of complex **1** against (a) *E. coli* and (b) *S. aureus*

Table 9. Antibacterial activity (inhibition zone diameter in mm) of synthesized complexes, precursor species, and controls against *E. coli* and *S. aureus*

Solution	Concentration		Inhibition zone (mm)	
	Mass (mg/mL)	Molar (mM)	*E. coli*(-)	*S. aureus*(+)
DMSO 10%(aq) (-)	-	-	0.00	0.00
$CoCl_2(H_2O–(CH_3)_2SO)$	5.00	21.01	13.59 ± 0.70	14.55 ± 0.57
$NiCl_2(H_2O–(CH_3)_2SO)$	5.00	21.04	11.08 ± 1.17	9.77 ± 0.93
3-ampy$(H_2O–(CH_3)_2SO)$	5.00	53.13	0.00 ± 0.00	0.00 ± 0.00
Na-Bz$(H_2O–(CH_3)_2SO)$	5.00	34.70	0.00 ± 0.00	0.00 ± 0.00
$[Co(3\text{-ampy})_2(Bz)_2(H_2O)]$ $(H_2O–(CH_3)_2SO)$ (**1**)	5.00	9.85	12.20 ± 0.44	13.67 ± 0.59
$[Ni(\mu\text{-}3\text{-ampy})_2(Bz)_2(H_2O)]_n$ $(H_2O–(CH_3)_2SO)$ (**2**)	5.00	12.11	4.90 ± 0.17	0.00 ± 0.00
Chloramphenicol (+)	-	-	25.20	25.80

In contrast, complex **1** produced smaller inhibition zones than its precursor cobalt(II) salt. This attenuated activity is primarily attributed to the larger molecular dimensions and hydrodynamic radius of the coordination complex relative to simple cobalt aquo ions, which restricts its passive diffusion rate through the agar matrix [47]. Thus, while complexation alters the structural and chemical identity of the metal species, it does not necessarily enhance agar diffusivity or bioactivity under the evaluated assay conditions. Although cobalt is an essential trace element integral to biological cofactors such as cobalamin (vitamin B12) [1], its essential physiological role cannot be directly extrapolated to explain the observed in vitro antibacterial efficacy of **1**.

Complex **2** displayed no detectable antibacterial activity against *S. aureus*. This lack of inhibition is strongly correlated with the physicochemical and structural properties of the complex. Hirshfeld surface analysis reveals that H···H contacts dominate the crystal surface, imparting a pronounced nonpolar, hydrophobic character. Moreover, complex **2** adopts a 1D polymeric chain architecture, where large molecular weight and extended structural connectivity severely hamper mobility and cellular uptake across the thick peptidoglycan cell wall characteristic of Gram-positive bacteria [48].

Notably, the amino ($-NH_2$) groups of 3-ampy, which typically serve as active antibacterial pharmacophores, are fully engaged in dative coordination to neighboring Ni(II) centers to construct the polymeric backbone. Their involvement in coordination diminishes their availability for electrostatically driven interactions with bacterial cell components or intracellular targets such as DNA. Consequently, restricted membrane permeation and limited target accessibility account for the inactivity of **2** against *S. aureus*.

Conversely, complex **2** exhibited weak but measurable activity against Gram-negative *E. coli*. This differential susceptibility reflects fundamental differences in cell envelope architecture between Gram-positive and Gram-negative species. *E. coli* possesses an outer lipopolysaccharide-rich membrane, a thin peptidoglycan layer, and an inner cytoplasmic membrane. Although the outer membrane functions as an effective permeability barrier against bulky hydrophobic molecules, the observed weak activity suggests that a minor fraction of the complex (or its dissociated species) crosses the cell envelope to reach intracellular target sites under the test conditions. However, because the disk diffusion assay measures macroscopic growth inhibition rather than uptake kinetics, specific translocation pathways and precise molecular mechanisms cannot be definitively assigned from these data alone.

Notably, complex **1** demonstrated larger inhibition zone diameters than its uncoordinated constituent ligands (3-ampy and Na-Bz) against both *E. coli* and *S. aureus* [1]. This enhancement highlights the crucial role of metal–ligand coordination in promoting bioactivity, a phenomenon broadly rationalized by Tweedy's chelation theory. Upon complexation, partial sharing of the metal ion's positive charge with donor atoms reduces metal polarity and promotes electron delocalization over the chelate ring [1]. Decreased polarity elevates the lipophilicity of the complex, facilitating its penetration through the lipid-rich bacterial cell membrane to disrupt cellular processes more effectively [23, 44].

Furthermore, the coordinated complex incorporates functional groups analogous to key moieties in chloramphenicol: carbonyl groups (from benzoate) capable of forming hydrogen bonds with nucleic acid bases, hydroxyl ligands (from water) capable of coordinating catalytic metal ions, and aromatic rings (from 3-ampy and benzoate) capable of engaging in π-stacking and C–H···π interactions with ribosomal residues [45]. Although sodium benzoate is a widely used food preservative, its isolated ligand solution produced no inhibition zone (0.00 mm), likely because its mass-equivalent concentration in the test solution was below the effective threshold required for bacterial inhibition [49].

3.4. Hirshfeld Surface Analysis

The molecular surfaces and 2D fingerprint plots generated from Hirshfeld surface calculations for complexes **1** and **2** are illustrated in Figures 18–21. As shown in the d_{norm} surfaces (Figures 18a and 19a), circular red regions highlight strong intermolecular interactions operating at distances shorter than the sum of the van der Waals radii, primarily corresponding to hydrogen-bonding networks. These close contact zones directly corroborate the bathochromic shifts observed for the N–H and O–H stretching vibrations in FTIR spectroscopy, as well as the geometry of hydrogen-bonding networks identified from SC-XRD crystal structure refinement using Mercury. Conversely, white regions denote contact distances equal to the sum of van der Waals radii, whereas blue regions represent longer, weaker intermolecular contacts [14, 23].

On the shape index surfaces (Figures 18b and 19b), convex red areas designate electron-accepting regions, while concave blue areas highlight electron-donating regions participating in intermolecular contacts. Crucially, complementary pairs of adjacent red and blue triangular regions serve as diagnostic indicators of aromatic π···π stacking interactions, whereas isolated red triangular patches signal C–H···π contacts. Both interaction types occur across the aromatic rings of 3-ampy and benzoate ligands, providing essential supramolecular stabilization to the crystal lattice [14, 23]. These non-covalent contacts play a vital role in biological recognition and cellular interactions [50]. In particular, π···π stacking interactions enhance overall complex hydrophobicity, facilitating passive translocation across the lipid bilayer of bacterial membranes. Moreover, these interactions reinforce intermolecular cohesion, conferring structural stability that minimizes premature degradation prior to reaching intracellular target sites [51]. Concurrently, C–H···π contacts serve as key directional forces directing the overall crystal packing arrangement [26].

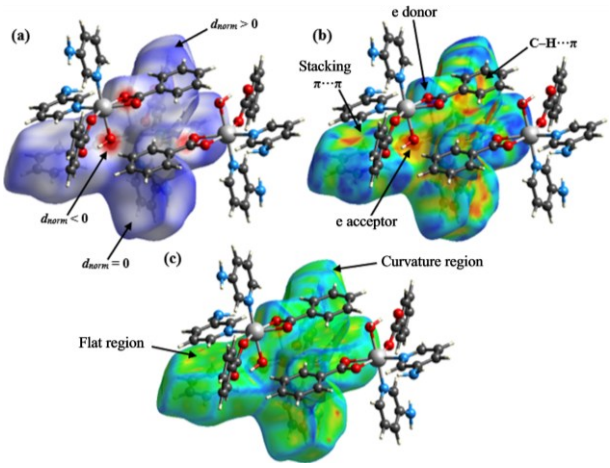


Figure 18. Hirshfeld surface analysis: (a) d_{norm} surface, (b) shape index, and (c) curvature of complex **1**

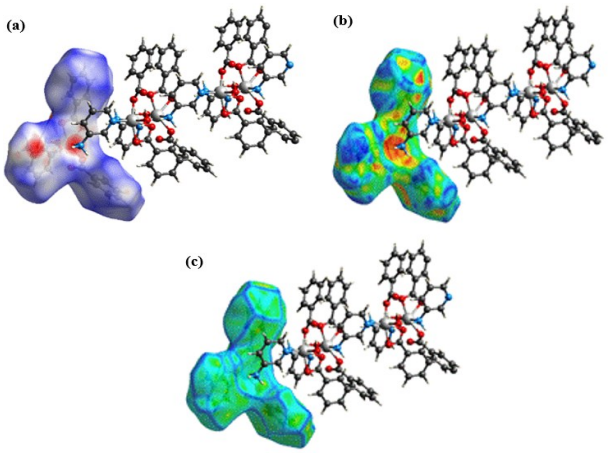


Figure 19. Hirshfeld surface analysis: (a) d_{norm} surface, (b) shape index, and (c) curvature of complex **2**

On the curvedness surfaces (Figures 18c and 19c), high-curvature regions are color-mapped in blue, whereas flat regions appear in green [23]. High-curvature (blue) domains reflect structural prominences that impede close molecular packing. In contrast, flat (green) regions correspond to planar molecular domains that facilitate close, parallel face-to-face packing, accommodating interplanar π···π stacking assemblies between adjacent complex units [14].

Figures 20 and 21 display the 2D fingerprint plots detailing the individual atomic contact contributions to the total Hirshfeld surface area for both complexes [52]. In both structures, H···H contacts constitute the single largest contribution, accounting for 48.0% of the surface area in complex **1** and 47.6% in complex **2**. The negligible difference (0.4%) between these values indicates that dispersion forces originating from nonpolar H···H interactions contribute almost identically to the crystal packing cohesion of both compounds. For both complexes, C···H/H···C interactions represent the second largest surface contribution, followed sequentially by O···H/H···O, C···C, and N···H/H···N contacts.

In the 2D fingerprint plots, O···H/H···O interactions are manifested as prominent, sharp, signifying short, highly directional interatomic contacts corresponding to classical intermolecular hydrogen bonds. Notably, the higher contribution of O···H/H···O contacts in complex **2** compared with complex **1** indicates a greater role of intermolecular hydrogen-bonding interactions in determining and stabilizing the crystal packing. Other minor contacts include N···H/H···N, Ni···N/N···Ni, C···O/O···C, N···O/O···N, C···N/N···C, and Ni···H/H···Ni [14].

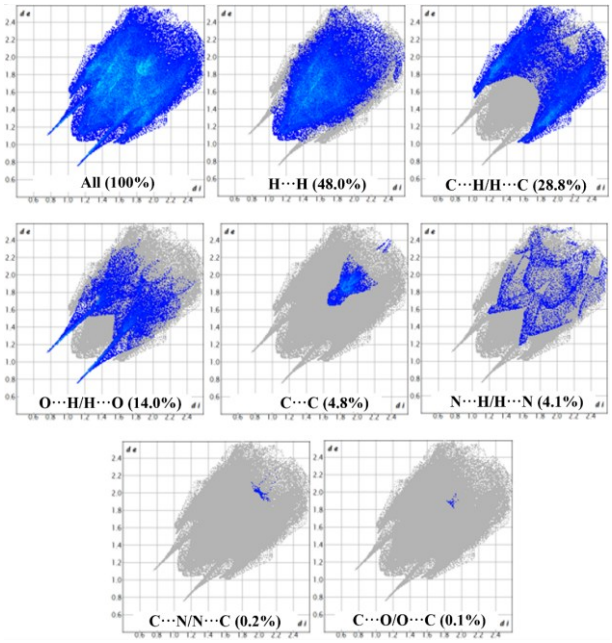


Figure 20. Plot fingerprint of complex **1**

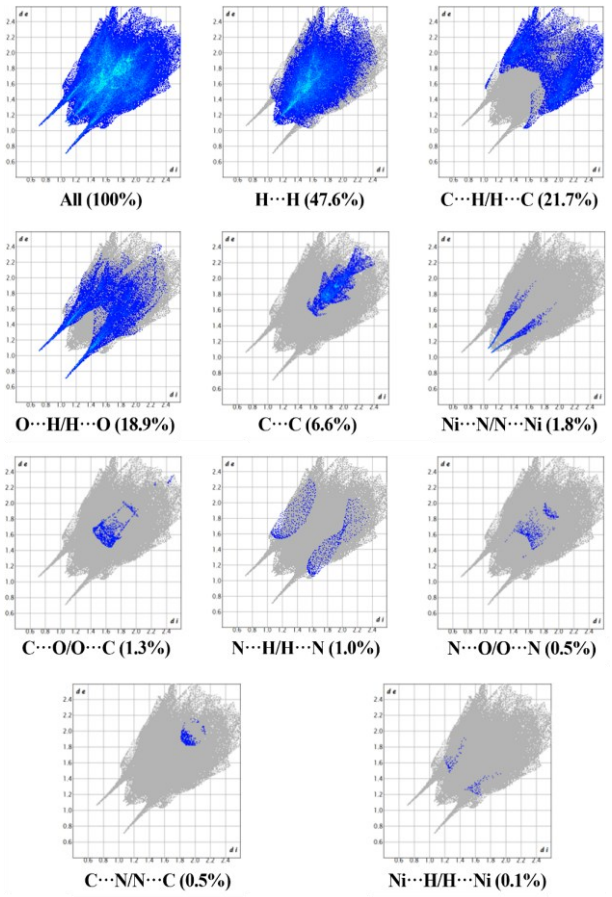


Figure 21. Plot fingerprint of complex **2**

4. Conclusion

Based on the results of this study, the complexes $[Co(3\text{-ampy})_2(Bz)_2(H_2O)]$ (**1**) and $[Ni(\mu\text{-}3\text{-ampy})_2(Bz)_2(H_2O)]_n$ (**2**) were successfully synthesized and characterized. Both complexes exhibited distorted octahedral coordination geometries and crystallized in the monoclinic crystal system. Although the same ligands were used, the two complexes exhibited different coordination architectures, with the cobalt(II) complex (**1**) adopting a monomeric structure and the nickel(II) complex (**2**) forming a polymeric structure. Antibacterial activity assays revealed that complex **1** exhibited greater antibacterial activity than complex **2** against *E. coli* and *S. aureus*, although both complexes showed lower activity than their respective metal salts. Complex **1** exhibited inhibition zone diameters of 12.20 and 13.67 mm against *E. coli* and *S. aureus*, respectively, whereas complex **2** produced an inhibition zone diameter of 4.90 mm against *E. coli* and showed no activity against *S. aureus*. Meanwhile, neither 3-ampy nor Na-Bz exhibited antibacterial activity. The differences in antibacterial activity between complexes **1** and **2** were associated with their distinct structural and physicochemical properties. Differences in coordination architecture may affect the size and mobility of the complex species, as well as their ability to diffuse through the agar medium. Although complex **2** exhibited greater thermal stability, as indicated by its higher melting point, it showed more limited antibacterial activity than complex **1**. These findings indicate that greater thermal stability does not necessarily translate into higher antibacterial activity.

Acknowledgment

The authors gratefully acknowledge Universitas Negeri Malang (UM), Indonesia, for financial support under the *Penelitian Pemula* scheme grant funded by UM's *Non-APBN* for the fiscal year 2025 (Contract No. 24.2.245/UN32.14.1/LT/2025). The authors also extend their gratitude to the Inorganic Chemistry Research Group at Universitas Negeri Malang for their invaluable support throughout this research.

References

[1] M. Claudel, J. V. Schwarte, K. M. Fromm, New Antimicrobial Strategies Based on Metal Complexes, *Chemistry*, 2, 4, (2020), 849-899 https://doi.org/10.3390/chemistry2040056

[2] M. W. Gach, G. Lazarus, D. M. Simadibrata, R. Sinto, Y. R. Saharman, R. Limato, E. J. Nelwan, H. R. van Doorn, A. Karuniawati, R. L. Hamers, Antimicrobial resistance among common bacterial pathogens in Indonesia: a systematic review, *The Lancet Regional Health - Southeast Asia*, 26, (2024), 100414 https://doi.org/10.1016/j.lansea.2024.100414

[3] C. J. L. Murray, K. S. Ikuta, F. Sharara, L. Swetschinski, G. Robles Aguilar, A. Gray, C. Han, C. Bisignano, P. Rao, E. Wool, S. C. Johnson, A. J. Browne, M. G. Chipeta, F. Fell, S. Hackett, G. Haines-Woodhouse, B. H. Kashef Hamadani, E. A. P. Kumaran, B. McManigal, S. Achalapong, R. Agarwal, S. Akech, S. Albertson, J. Amuasi, J. Andrews, A. Aravkin, E. Ashley, F.-X. Babin, F. Bailey, S. Baker, B. Basnyat, A. Bekker, R. Bender, J. A. Berkley, A. Bethou, J. Bielicki, S. Boonkasidecha, J. Bukosia, C. Carvalheiro, C. Castañeda-Orjuela, V. Chansamouth, S. Chaurasia, S. Chiurchiù, F. Chowdhury, R. Clotaire Donatien, A. J. Cook, B. Cooper, T. R. Cressey, E. Criollo-Mora, M. Cunningham, S. Darboe, N. P. J. Day, M. De Luca, K. Dokova, A. Dramowski, S. J. Dunachie, T. Duong Bich, T. Eckmanns, D. Eibach, A. Emami, N. Feasey, N. Fisher-Pearson, K. Forrest, C. Garcia, D. Garrett, P. Gastmeier, A. Z. Giref, R. C. Greer, V. Gupta, S. Haller, A. Haselbeck, S. I. Hay, M. Holm, S. Hopkins, Y. Hsia, K. C. Iregbu, J. Jacobs, D. Jarovsky, F. Javanmardi, A. W. J. Jenney, M. Khorana, S. Khusuwan, N. Kissoon, E. Kobeissi, T. Kostyanev, F. Krapp, R. Krumkamp, A. Kumar, H. H. Kyu, C. Lim, K. Lim, D. Limmathurotsakul, M. J. Loftus, M. Lunn, J. Ma, A. Manoharan, F. Marks, J. May, M. Mayxay, N. Mturi, T. Munera-Huertas, P. Musicha, L. A. Musila, M. M. Mussi-Pinhata, R. N. Naidu, T. Nakamura, R. Nanavati, S. Nangia, P. Newton, C. Ngoun, A. Novotney, D. Nwakanma, C. W. Obiero, T. J. Ochoa, A. Olivas-Martinez, P. Olliaro, E. Ooko, E. Ortiz-Brizuela, P. Ounchanum, G. D. Pak, J. L. Paredes, A. Y. Peleg, C. Perrone, T. Phe, K. Phommasone, N. Plakkal, A. Ponce-de-Leon, M. Raad, T. Ramdin, S. Rattanavong, A. Riddell, T. Roberts, J. V. Robotham, A. Roca, V. D. Rosenthal, K. E. Rudd, N. Russell, H. S. Sader, W. Saengchan, J. Schnall, J. A. G. Scott, S. Seekaew, M. Sharland, M. Shivamallappa, J. Sifuentes-Osornio, A. J. Simpson, N. Steenkeste, A. J. Stewardson, T. Stoeva, N. Tasak, A. Thaiprakong, G. Thwaites, C. Tigoi, C. Turner, P. Turner, H. R. van Doorn, S. Velaphi, A. Vongpradith, M. Vongsouvath, H. Vu, T. Walsh, J. L. Walson, S. Waner, T. Wangrangsimakul, P. Wannapinij, T. Wozniak, T. E. M. W. Young Sharma, K. C. Yu, P. Zheng, B. Sartorius, A. D. Lopez, A. Stergachis, C. Moore, C. Dolecek, M. Naghavi, Global burden of bacterial antimicrobial resistance in 2019: a systematic analysis, *The Lancet*, 399, 10325, (2022), 629-655 https://doi.org/10.1016/S0140-6736(21)02724-0

[4] J. E. Waters, L. Stevens-Cullinane, L. Siebenmann, J. Hess, Recent advances in the development of metal complexes as antibacterial agents with metal-specific modes of action, *Current Opinion in Microbiology*, 75, (2023), 102347 https://doi.org/10.1016/j.mib.2023.102347

[5] G. K. Bunduki, E. Heinz, V. S. Phiri, P. Noah, N. Feasey, J. Musaya, Virulence factors and antimicrobial resistance of uropathogenic *Escherichia coli* (UPEC) isolated from urinary tract infections: a systematic review and meta-analysis, *BMC Infectious Diseases*, 21, (2021), 753 https://doi.org/10.1186/s12879-021-06435-7

[6] A. Al Emon, H. Hossain, M. S. R. Chowdhury, M. A. Rahman, F. Y. Tanni, M. N. Asha, H. Akter, M. M. Hossain, M. R. Islam, M. M. Rahman, Prevalence, antimicrobial susceptibility profiles and resistant gene identification of bovine subclinical mastitis pathogens in Bangladesh, *Heliyon*, 10, 14, (2024), e34567 https://doi.org/10.1016/j.heliyon.2024.e34567

[7] C. Lv, J. Leng, M. Qian, B. Sun, H. P. Ye, M. Li, N. Zhou, Z. Cheng, Y. Chen, X. Guo, J. Shang, L. Zhang, Y. Zhu, Antimicrobial Resistance in *Escherichia coli* and *Staphylococcus aureus* at Human-Animal Interfaces on Chongming Island, Shanghai: A One Health Perspective, *One Health*, 19, (2024), 100910 https://doi.org/10.1016/j.onehlt.2024.100910

[8] B. Sharma, S. Shukla, R. Rattan, M. Fatima, M. Goel, M. Bhat, S. Dutta, R. K. Ranjan, M. Sharma, Antimicrobial Agents Based on Metal Complexes: Present Situation and Future Prospects, *International Journal of Biomaterials*, 2022, (2022), 6819080 https://doi.org/10.1155/2022/6819080

[9] G. Gasser, N. Metzler-Nolte, The potential of organometallic complexes in medicinal chemistry, *Current Opinion in Chemical Biology*, 16, 1-2, (2012), 84-91 https://doi.org/10.1016/j.cbpa.2012.01.013

[10] F. S. M. Hassan, M. Fayez, N. Abdalla, Synthesis, Characterization, Antibacterial, and Antifungal Activities of Cobalt(II), Nickel(II) and Copper(II) Complexes with 3-thioacetyl-2-amino-1,4-naphthoquinone and 2-benzoyl-3-amino-1,4-naphthoquinone Ligands, *Open Journal of Inorganic Non-metallic Materials*, 10, 4, (2020), 45-61 https://doi.org/10.4236/ojinm.2020.104004

[11] N. Vamsikrishna, M. P. Kumar, S. Tejaswi, A. Rambabu, Shivaraj, DNA Binding, Cleavage and Antibacterial Activity of Mononuclear Cu(II), Ni(II) and Co(II) Complexes Derived from Novel Benzothiazole Schiff Bases, *Journal of Fluorescence*, 26, 4, (2016), 1317-1329 https://doi.org/10.1007/s10895-016-1818-z

[12] M. S. Al-Fakeh, G. A. Allazzam, N. H. Yarkandi, Ni(II), Cu(II), Mn(II), and Fe(II) Metal Complexes Containing 1,3-Bis(diphenylphosphino)propane and Pyridine Derivative: Synthesis, Characterization, and Antimicrobial Activity, *International Journal of Biomaterials*, 2021, (2021), 4981367 https://doi.org/10.1155/2021/4981367

[13] A. Munadhiroh, H. W. Wijaya, N. Farida, S. Golhen, I. W. Dasna, Synthesis, Characterization, and Preliminary Study of $[Co(2\text{-aminopyridine})_2(NCS)_2]$ or bis(2-aminopyridine)dithiocyanato cobalt(II) as An Antibacterial, *Jurnal Kimia Valensi*, 8, 1, (2022), 23-29 https://doi.org/10.15408/jkv.v8i1.22685

[14] L. A. Savitri, F. S. Putra, S. D. Laksmana, D. Mariyam, I. W. Dasna, Synthesis, Structure, Antibacterial Activity, and Hirshfeld Surface Analysis of Complex $[Co(4\text{-ampy})_4(NCS)_2]\cdot CO_2$, *Indonesian Journal of Chemistry*, 24, 4, (2024), 1046-1057 https://doi.org/10.22146/ijc.90585

[15] S. Devraye, S. Jadhav, S. Zangade, Preparation, structure elucidation, free radical scavenging, *in-vitro* antimicrobial and cytotoxic proficiency of isoniazid incorporated tridentate Co(II), Ni(II), Cu(II) and Zn(II) Schiff base-metal complexes, *Results in Chemistry*, 16, (2025), 102407 https://doi.org/10.1016/j.rechem.2025.102407

[16] I. Elaaraj, N. Moukrad, A. Bouymajane, S. Er Raouan, A. Nakkabi, O. Oulidi, F. Rhazi Filai, I. Koraichi Saad, F. Cacciola, N. El Moualij, M. Fahim, Elaboration and structural study of Ni(II), Cu(II), Zn(II) and Co(II) complexes based on the ligand [(N1Z,N2Z)-N1,N2-bis((1H-pyrrol-2-yl) methylene) ethane-1,2-diamine] with evaluation of antioxidant/antibacterial activities and cytotoxicity, *Results in Chemistry*, 5, (2023), 100787 https://doi.org/10.1016/j.rechem.2023.100787

[17] Z. Kartal, O. Şahin, The synthesis of heteroleptic cyanometallate aminopyridine complexes and an investigation into their structural properties with various spectroscopic methods, *Journal of Molecular Structure*, 1227, (2021), 129514 https://doi.org/10.1016/j.molstruc.2020.129514

[18] J. V. Handy, G. Ayala, R. D. Pike, Structural comparison of copper(II) thiocyanate pyridine complexes, *Inorganica Chimica Acta*, 456, (2017), 64-75 https://doi.org/10.1016/j.ica.2016.11.013

[19] B. Dojer, A. Pevec, M. Jagodič, M. Kristl, M. Drofenik, Three new cobalt(II) carboxylates with 2-, 3- and 4-aminopyridine: Syntheses, structures and magnetic properties, *Inorganica Chimica Acta*, 383, (2012), 98-104 https://doi.org/10.1016/j.ica.2011.10.056

[20] F. A. Mautner, P. V. Jantscher, R. C. Fischer, A. Torvisco, K. Reichmann, S. S. Massoud, Syntheses, structural characterization, and thermal behaviour of metal complexes with 3-aminopyridine as co-ligands, *Transition Metal Chemistry*, 46, (2021), 191-200 https://doi.org/10.1007/s11243-020-00436-2

[21] A. A. Alsudani, In vitro antifungal effect of potassium sorbate and sodium benzoate on the growth of fungi causing sinusitis, *African Journal of Microbiology Research*, 11, 6, (2017), 232-236 https://doi.org/10.5897/ajmr2016.8414

[22] O. C. S. Montilva, F. Movilla, M. G. Rodriguez, F. Di Salvo, Synthesis, crystal structure and study of the crystal packing in the complex bis-(4-amino-pyridine-κN^1)di-chlorido-cobalt(II), *Acta Crystallographica Section C: Structural Chemistry*, C73, (2017), 399-406 https://doi.org/10.1107/S2053229617004880

[23] H. W. Wijaya, G. C. Nugraha, V. D. Alfian, U. S. F. Arrozi, M. E. F. Sari, S. D. Laksmana, F. S. Putra, I. W. Dasna, Synthesis, structure, hirshfeld surface analysis and antibacterial activities of $[Cd(2\text{-ampy})_3(NCS)(\mu_{1,5}\text{-SCN})]_2$ and $[Cd(4\text{-ampy})_2(\mu_{1,5}\text{-dca})_2]_n$ complexes (2-ampy = 2-aminopyridine, 4-ampy = 4-aminopyridine, NCS = thiocyanate, dca = dicyanamide), *Chemistry of Inorganic Materials*, 3, (2024), 100054 https://doi.org/10.1016/j.cinorg.2024.100054

[24] I. Darsaklis, Identification of an Unknown Organic Compound by Determination of its Melting Point, *International Journal of Scientific Research in Chemical Sciences*, 12, 1, (2025), 28-32 https://doi.org/10.26438/ijsrcs.v12i1.184

[25] P. D. Lestari, N. Farida, I. W. Dasna, Synthesis, Structure, Hirshfeld Surface Analysis, and Antibacterial Activity of $[Ni(3\text{-}NH_2py)_4Cl_2]$ Complex (3-NH_2py = 3-aminopyridine), *Jurnal Kimia Sains dan Aplikasi*, 28, 3, (2025), 106-114 https://doi.org/10.14710/jksa.28.3.106-114

[26] K. K. Dutta, T. Baishya, R. M. Gomila, A. Frontera, M. Barcelo-Oliver, A. K. Verma, J. Das, M. K. Bhattacharyya, Supramolecular Assemblies and Anticancer Activities of Aminopyridine-Based Polynuclear and Mononuclear Co(II) Benzoates: Experimental and Theoretical Studies, *Inorganics*, 13, 2, (2025), 51 https://doi.org/10.3390/inorganics13020051

[27] P. Paul, S. Roy, S. Sarkar, S. Chowdhury, R. N. D. Purkayastha, P. Raghavaiah, P. McArdle, L. Deb, S. I. Devi, Synthesis, structure and some properties of a manganese(II) benzoate containing diimine, *Journal of Molecular Structure*, 1102, (2015), 153-160 https://doi.org/10.1016/j.molstruc.2015.08.049

[28] B. Shirley, E. Jarochowska, Chemical characterisation is rough: the impact of topography and measurement parameters on energy-dispersive X-ray spectroscopy in biominerals, *Facies*, 68, (2022), 7 https://doi.org/10.1007/s10347-022-00645-4

[29] A. W. Bauer, W. M. M. Kirby, J. C. Sherris, M. Turck, Antibiotic Susceptibility Testing by a Standardized Single Disk Method, *American Journal of Clinical Pathology*, 45, 4, (1966), 493-496 https://doi.org/10.1093/ajcp/45.4_ts.493

[30] CLSI, *Performance Standards for Antimicrobial Disk Susceptibility Tests*, 14th ed., Clinical and Laboratory Standards Institute, 2024,

[31] E. P. Casman, R. W. Bennett, A. E. Dorsey, A. J. A. Issa, Identification of a Fourth Staphylococcal Enterotoxin, Enterotoxin D, *Journal of Bacteriology*, 94, 6, (1967), 1875-1882 https://doi.org/10.1128/jb.94.6.1875-1882.1967

[32] M. S. Islam, I. Gupta, E. T. Farinas, S. Mitra, Enhancing the Solubility and Antibacterial Efficacy of Sulfamethoxazole by Incorporating Functionalized PLGA and Graphene Oxide Nanoparticles into the Crystal Structure, *Pharmaceutics*, 17, 11, (2025), 1460 https://doi.org/10.3390/pharmaceutics17111460

[33] H. Fang, X. Li, W. Sun, C. Wang, N. Chen, Y. Gan, J. Huang, Y. Ma, H. Tanaka, P. Tan, Dual-symmetry-guided assembly of complex lattices, *Nature*, 652, (2026), 635-642 https://doi.org/10.1038/s41586-026-10364-3

[34] I. W. Dasna, D. Mariyam, H. W. Wijaya, U. S. F. Arrozi, S. Sugiarto, Synthesis, Structural Determination and Antibacterial Properties of Zinc(II) Complexes Containing 4-Aminopyridine Ligands, *Indonesian Journal of Chemistry*, 23, 4, (2023), 1108-1119 https://doi.org/10.22146/ijc.82801

[35] T. Seki, K. Y. Chiang, C. C. Yu, X. Yu, M. Okuno, J. Hunger, Y. Nagata, M. Bonn, The Bending Mode of Water: A Powerful Probe for Hydrogen Bond Structure of Aqueous Systems, *Journal of Physical Chemistry Letters*, 11, 19, (2020), 8459-8469 https://doi.org/10.1021/acs.jpclett.0c01259

[36] M. Scimeca, S. Bischetti, H. K. Lamsira, R. Bonfiglio, E. Bonanno, Energy Dispersive X-ray (EDX) microanalysis: A powerful tool in biomedical research and diagnosis, *European Journal of Histochemistry*, 62, 1, (2018), 2841 https://doi.org/10.4081/ejh.2018.2841

[37] R. Freitag, J. Conradie, Understanding the Jahn-Teller Effect in Octahedral Transition-Metal Complexes: A Molecular Orbital View of the Mn(β-diketonato)$_3$ Complex, *Journal of Chemical Education*, 90, 12, (2013), 1692-1696 https://doi.org/10.1021/ed400370p

[38] C. Janiak, A critical account on π−π stacking in metal complexes with aromatic nitrogen-containing ligands, *Journal of the Chemical Society, Dalton Transactions*, 29, 21, (2000), 3885-3896 https://doi.org/10.1039/b0030100

[39] Y. Sohtome, G. Nakamura, A. Muranaka, D. Hashizume, S. Lectard, T. Tsuchimoto, M. Uchiyama, M. Sodeoka, Naked *d*-orbital in a centrochiral Ni(II) complex as a catalyst for asymmetric [3+2] cycloaddition, *Nature Communications*, 8, (2017), 14875 https://doi.org/10.1038/ncomms14875

[40] D. Dutta, R. Dubey, S. K. Dwivedi, A. Puzari, Colorimetric Detection of Cobalt in Different Solvents by Using Their Solvatochromic Properties, *Saudi Journal of Engineering and Technology*, 5, 4, (2020), 144-149 https://doi.org/10.36348/sjet.2020.v05i04.003

[41] R. Fouad, I. A. Shaaban, T. E. Ali, M. A. Assiri, S. S. Shenouda, Co(II), Ni(II), Cu(II) and Cd(II)-thiocarbonohydrazone complexes: spectroscopic, DFT, thermal, and electrical conductivity studies, *RSC Advances*, 11, 60, (2021), 37726-37743 https://doi.org/10.1039/d1ra06902k

[42] B. Rahardjo, D. M. Wijanarko, R. Astuti, A. A. Martina, Synthesis and characterization of diaquadinicotinamide cobalt(II) chloride, *International Conference on Science and Applied Science (ICSAS) 2018*, Surakarta, Indonesia, 2018 https://doi.org/10.1063/1.5054414

[43] M. L. Bols, J. Ma, F. Rammal, D. Plessers, X. Wu, S. Navarro-Jaén, A. J. Heyer, B. F. Sels, E. I. Solomon, R. A. Schoonheydt, *In Situ* UV−Vis−NIR Absorption Spectroscopy and Catalysis, *Chemical Reviews*, 124, 5, (2024), 2352−2418 https://doi.org/10.1021/acs.chemrev.3c00602

[44] A. C. B. Yuoh, M. O. Agwara, D. M. Yufanyi, M. A. Conde, R. Jagan, K. O. Eyong, Synthesis, Crystal Structure, and Antimicrobial Properties of a Novel 1-D Cobalt Coordination Polymer with Dicyanamide and 2-Aminopyridine, *International Journal of Inorganic Chemistry*, 2015, (2015), 1-8 https://doi.org/10.1155/2015/106838

[45] L. Xue, C. M. T. Spahn, M. Schacherl, J. Mahamid, Structural insights into context-dependent inhibitory mechanisms of chloramphenicol in cells, *Nature Structural & Molecular Biology*, 32, 2, (2025), 257-267 https://doi.org/10.1038/s41594-024-01441-0

[46] O. N. Kostopoulou, G. E. Magoulas, G. E. Papadopoulos, A. Mouzaki, G. P. Dinos, D. Papaioannou, D. L. Kalpaxis, Synthesis and Evaluation of Chloramphenicol Homodimers: Molecular Target, Antimicrobial Activity, and Toxicity Against Human Cells, *PLoS One*, 10, 8, (2015), e0134526 https://doi.org/10.1371/journal.pone.0134526

[47] A. Menichetti, A. Mavridi-Printezi, D. Mordini, M. Montalti, Effect of Size, Shape and Surface Functionalization on the Antibacterial Activity of Silver Nanoparticles, *Journal of Functional Biomaterials*, 14, 5, (2023), 244 https://doi.org/10.3390/jfb14050244

[48] F. Riu, A. Ruda, R. Ibba, S. Sestito, I. Lupinu, S. Piras, G. Widmalm, A. Carta, Antibiotics and Carbohydrate-Containing Drugs Targeting Bacterial Cell Envelopes: An Overview, *Pharmaceuticals*, 15, 8, (2022), 942 https://doi.org/10.3390/ph15080942

[49] L. Hejazi, M. Mahboubi-Rabbani, V. Mahdavi, M. Alemi, E. Khanniri, M. Bayanati, A critical review on sodium benzoate from health effects to analytical methods, *Results in Chemistry*, 11, (2024), 101798 https://doi.org/10.1016/j.rechem.2024.101798

[50] J. S. Dhau, A. Singh, A. Singh, B. S. Sooch, P. Brandão, V. Félix, Synthesis and antibacterial activity of

pyridylselenium compounds: Self-assembly of bis(3-bromo-2-pyridyl)diselenide via intermolecular secondary and π···π stacking interactions, *Journal of Organometallic Chemistry*, 766, (2014), 57-66 https://doi.org/10.1016/j.jorganchem.2014.05.009

[51] W. R. Zhuang, Y. Wang, P. F. Cui, L. Xing, J. Lee, D. Kim, H. L. Jiang, Y. K. Oh, Applications of π-π stacking interactions in the design of drug-delivery systems, *Journal of Controlled Release*, 294, (2019), 311-326 https://doi.org/10.1016/j.jconrel.2018.12.014

[52] O. Ben Moussa, H. Chebbi, M. F. Zid, Synthesis, crystal structure, vibrational study, optical properties and Hirshfeld surface analysis of bis(2,6-diaminopyridinium) tetrachloridocobaltate(II) monohydrate, *Journal of Molecular Structure*, 1180, (2019), 72-80 https://doi.org/10.1016/j.molstruc.2018.11.077